www.sciencemag.org/cgi/content/full/1170371/DC1

Supporting Online Material for

Evidence for Obliquity Forcing of Glacial Termination II

R. N. Drysdale,* J. C. Hellstrom, G. Zanchetta, A. E. Fallick, M. F. Sánchez Gõni, I. Couchoud, J. McDonald, R. Maas, G. Lohmann, I. Isola

*To whom correspondence should be addressed. E-mail: russell.drysdale@newcastle.edu.au

Published 13 August 2009 on *Science* Express
DOI: 10.1126/science.1170371

This PDF file includes:

Supplementary Online Material – Drysdale et al.

1. MATERIALS AND METHODS

The studied stalagmite sections comprised compact, faintly laminated calcite with no signs of mineral alteration. Table S1 summarizes the depth and corresponding ages of sections for high-resolution stable isotope analyses, together with the number of isotope and age data points for each. Age coverage is shown graphically in Figure S2. The most complete and detailed sequence was obtained from stalagmite CC5. Approximately 84% of the period 120 -145 ky contains overlapping growth (Figure S2) from one other stalagmite. Time series from overlapping portions show good correspondence with CC5, indicating that the isotopic behavior of these stalagmites and the radiometric dating are sound (Figure S3).

We reported in a previous low-resolution study of CC5 *(ref S1)* that this stalagmite grew continuously between ~170-90 ky. After re-sampling this stalagmite at high-resolution and further U/Th dating we now find evidence for a growth interruption between ca. 125.4 and 123.5 ky. Most of this break is spanned by a growth phase in stalagmite CC7, leaving a period of only ca. 500 years without representation. The cause of the hiatus is indeterminate: although climate may be responsible, the likely mechanism(s) is not obvious because it occurs shortly after the Last Interglacial optimum. Given that the area is seismically active, an earthquake-induced disruption to the fracture/flow network is a possibility. Either way, it occurs well after Termination II and does not affect the conclusions drawn from our work.

All stalagmite sections displayed sufficiently wide zones (3 - 10 mm) of tabular, parallel lamination patterns well-suited to microsampling by a milling lathe, which follows a previously described method *(ref S2)*. Briefly, target sections were cut into multiple overlapping slabs ca. 3 – 5 mm thick, embedded in clear casting resin and milled using a Taig CNC micromilling lathe. All sampling was conducted at 100 μm increments. We applied a very conservative estimate of the maximum sampling error of ±200 μm from the midpoint of each 100 μm layer, giving an effective sampling interval of 100 ± 150 μm. However, in most of the calcite sections lamination patterns were clear and the sampling error is unlikely to exceed ± 100 μm from the midpoint (i.e. 100 ± 50 μm).

Results of low-resolution stable isotope measurements for CC1 and CC5 were published previously *(refs S1, S3)*. The depth scales here differ to those reported earlier because we conducted our microsampling along slightly different segments represented by the same growth phases. New stable isotope ($\delta^{18}O$ and $\delta^{13}C$) measurements were performed on ~1 mg powders using continuous-flow isotope-ratio mass spectrometry. Measurements were made on two identical mass spectrometers, an Analytical Precision AP2003 at the Scottish Universities Environmental Research Centre, East Kilbride UK, and a GV Instruments GV2003 (GVI's successor to the AP2003) at the Advanced Mass Spectrometry Unit, The University of Newcastle, Australia. Samples were digested in 105% phosphoric acid at 70°C. Mass spectrometric measurements were made on the evolved CO_2 gas. Results were normalized to the Vienna Pee Dee Belemnite scale using internal working standards of Carrara Marble (MAB1 – East Kilbride; NEW1 – Newcastle), which were cross-checked against the international standards NBS18 and NBS19. Mean analytical precision for both $\delta^{18}O$ and $\delta^{13}C$ is better than 0.1‰. Replicate measurements were made in all cases where adjacent sample results differed by ≥0.4‰.

2. SUPPORTING TEXT

2a. Stable isotope interpretation

Recent reviews (*ref S4–S5*) have highlighted the complex factors that drive speleothem $\delta^{18}O$. However, our previous studies of Corchia speleothems (*ref S1–S3*) show a consistent pattern where $\delta^{18}O$ tracks changes in regional temperatures. We argue that the mechanism that links regional temperatures to the speleothem $\delta^{18}O$ is rainfall amount, whereby warmer SSTs during regional temperature increases give rise to higher amounts of rainfall reaching the cave site, and *vice versa*. We suspect this is accentuated at Corchia because the NW-SE aligned mountain belt (the Alpi Apuane) that hosts the cave reaches almost 2000 m and acts as a major orographic barrier to air masses sweeping across SW Europe and the Mediterranean from the North Atlantic (*ref S6*). Today, mean rainfall above Corchia Cave exceeds 3000 mm, making the region one of the wettest in Europe. Local rainfall-$\delta^{18}O$ relationships for northwestern Italy using International Atomic Energy Agency's *Global Network for Istopes in*

Precipitation (GNIP) data show that rainfall amount is an important driver of rainfall $\delta^{18}O$ (*ref S7*). Orographic effects in the Alpi Apuane would accentuate this.

Other Corchia speleothem properties overwhelmingly support this interpretation of $\delta^{18}O$ as a rainfall amount proxy:

Growth rates: These should increase as the amount of percolation water (i.e. rainfall) reaching the speleothem increases (*ref S11*). Thus, other things being equal, growth rates and $\delta^{18}O$ should move together. A comparison between growth rates and Corchia $\delta^{18}O$ bears this out to some extent (Figure S4a). However, other factors besides rainfall impinge upon growth rates, particularly during large-scale climate shifts such as a glacial termination. Most notable of these is temperature through its control of vegetation activity and soil CO_2 production, the latter of which enhances the Ca^{2+} load of drip waters, a key growth-rate driver (*ref S11–S12*). Given our SST-rainfall amount-$\delta^{18}O$ argument above, this would *still* produce covarying speleothem $\delta^{18}O$ and growth rates. However, post-glacial soil and vegetation recovery above Corchia appears to be slow during glacial-interglacial transitions, as shown by the consistently 'sluggish' interglacial recovery of $\delta^{13}C$: 'optimum' $\delta^{13}C$ values (i.e. the most negative, which most likely reflect the largest inputs of soil CO_2) lag early interglacial 'climatic optima' by up to 10,000 years (see supplementary information in *ref S2*). Through T-II, growth rates also follow the major features of $\delta^{13}C$ (Figure S4b), perhaps better than they do for $\delta^{18}O$. In summary, the Corchia growth rates follow the main features of both $\delta^{18}O$ and $\delta^{13}C$, providing good support that $\delta^{18}O$ is an SST-linked rainfall-amount proxy. The lagged soil recovery above the cave is a scientifically sound reason why the growth rate-$\delta^{18}O$ relationship is not stronger.

Trace elements: Further support for the interpretation of the $\delta^{18}O$ comes from trace element data, which were derived from analyses conducted on a polished section of CC5 spanning T-II. We used excimer laser-ablation inductively coupled plasma mass spectrometry (LA-ICP-MS) at the University of Melbourne and measured Ca, Mg, P, Ba, Fe, Mn, Sr, U and Th using a raster scanning technique described by *ref S13*. Prior to analysis, the calcite surface was precleaned by ultrasonication for 15 minutes. Two laser scans, 3 mm apart, were made to check data replicability. Each scan line was pre-ablated twice at 10 Hz to remove residual surface contaminants using a rectangular slit of 250 $\mu m \times 50$ μm and employing a scan speed of 20 mm min^{-1}. For the sample data collection, the slit size and scan speed were reduced to 150 $\mu m \times 25$ μm and 1.2 mm min^{-1} respectively. The NIST612 glass standard was ablated before, during and after the calcite block, and was used to convert calcite sample intensities to concentrations in ppm. Absolute uncertainties due to differences in elemental fractionation between the NIST glass and calcite are no more than 10%.

Raw data were processed using the LA-ICP-MS software package "Iolite" (*ref S13*). Here we focus on results for Mg and U, two potential paleohydrological proxies (*ref S13–S15*); previous work on Corchia speleothems (*ref S16*) has revealed that both elements consistently track patterns of $\delta^{18}O$ changes.

The results from T-II are shown in Figures S5a and S5b. Both Mg and U trace element results yielded very good reproducibility (Figure S6). Mg in speleothems is a well known palaeohydrological proxy, with higher concentrations confined to drier climatic phases due primarily to 'prior calcite precipitation' (PCP) occurring along dewatered fractures and/or during incongruent dissolution of dolomite (*ref S15*). The depth of the cave chamber below the ground surface (400 m), and thus the long travel times for percolation waters, favors PCP under drier phases (*ref 15*). However, the high Mg/Ca molar ratios (>1; *ref S6*) observed in modern Corchia drip waters, the low Ca values of both drip and spring waters at similar-altitude sites throughout the region, and the predominantly dolomitic lithology hosting this section of the cave system strongly favor incongruent dissolution over PCP. During wetter phases, when water residence times are shorter, the effect of incongruent dissolution on drip water Mg/Ca would be reduced, leading to lower Mg concentrations in the speleothems. The Mg follows the main structural variations in $\delta^{18}O$ (Figure S5a). The positive relationship between the two parameters lends strong support to $\delta^{18}O$ being forced predominantly by rainfall amount.

Factors affecting uranium variations are not as well understood as Mg, hence fewer studies have used it as a speleothem climate proxy. However, as Figure S5b shows, changes in U concentrations also track the major changes in $\delta^{18}O$ through T-II, but the relationship is negative: greater U concentrations generally occur when $\delta^{18}O$ is lower (i.e. higher rainfall). U is readily leached under oxidising conditions (*ref 17*), so its release should increase during wet climatic stages. Treble et al. (*ref S14*) found a similar relationship between speleothem U and rainfall amount although they linked high U periods with elevated phosphorous leached from the overlying soil during wetter periods fo the year. Whilst the overall significance of U geochemistry of speleothems remains poorly understood, it is nonetheless clear that it is predominantly controlled by hydrological factors (*ref S14*).

Uranium isotope activity ratios: Speleothem uranium isotope activity ratios ($[^{234}U/^{238}U]_i$) can increase during dry climatic phases due to alpha recoil, which preferentially releases bedrock ^{234}U into relatively static, long-residence-time percolation waters that are at ~equilibrium with the bedrock (*ref S18*). During wetter phases, percolation is more rapid and dissolution rates greater, so both U isotopes are leached ~equally from the bedrock. This leads to lower $[^{234}U/^{238}U]_i$ compared to dry times. Comparison between Corchia $\delta^{18}O$ and $[^{234}U/^{238}U]_i$ shows an increase between ~141 and ~130 ky (Figure S7) when $\delta^{18}O$ is higher and growth rates lower, which is consistent with lower rainfall and cooler SSTs during this interval.

Notwithstanding the above arguments, the interpretation of past speleothem $\delta^{18}O$ is complex and must take account of other hydrological and physical processes, such as changes in air mass trajectories, composition and source of vapor (including ice-volume changes to ocean water $\delta^{18}O$), seasonal distribution of rainfall, and air temperatures.

Although elsewhere shifts in these variables may be important, modeling results relevant to western Italy (*ref S7*) show that vapor source (i.e. the proportion of Atlantic and Mediterranean sourced rainfall) varies little under interglacial, glacial and intermediate climate states, and that the rainfall amount is a persistent influence on $\delta^{18}O$. Furthermore, the air temperature effect at our mid-latitude site (whereby higher temperatures give rise to higher rainfall $\delta^{18}O$) is approximately cancelled out by the cave temperature fractionation effect (whereby the $\delta^{18}O$ of precipitated calcite at a given drip water $\delta^{18}O$ decreases as cave temperature [a proxy for mean annual temperature] increases), a phenomenon which modelling shows (*ref. S7*) applies to glacial, interglacial and intermediate climate states for our region. The effect of changes in the seasonality of precipitation can also be important. For example, Longinelli et al. (*ref. S8*) showed that during 2003, an extreme year in terms of summer temperatures and below-average summer rainfall, the annual weighted mean $\delta^{18}O$ value of precipitation was significantly lower due to a bias towards the winter contribution to the annual total. However, whether or not such an isotopic anomaly would persist during a similar climatic state but of millennical-scale duration (as opposed to a single extreme year) is debatable because the long-term climate boundary conditions would be different.

Finally, the influence of Sapropel S5 on the speleothem $\delta^{18}O$ must also be considered. A clear signature for part of the most recent sapropel (S1) has already been observed in a Corchia stalagmite (CC26; *ref.S9*). This was linked to increased rainfall, and produced a modest excursion of only ca -0.4 ‰. Although S5 was a more persistent sapropel, it commenced well after the start of deglaciation, and indeed after the T-II midpoint, and, judging by the planktic $\delta^{18}O$ and SST signatures in the eastern Mediterranean, reached its most intense phase during the thermal optimum (*ref. S10*). Thus, the timing and likely magnitude of its contribution (based on the anomaly observed for S1 – *ref. S9*) suggests it has little bearing on the synchronization of the marine sequence to the speleothem record.

2b. Uranium-thorium dating

The isotope time series from each of the three stalagmites were anchored by a total of 56 U/Th ages (Table S1), all of which were determined using a Nu Instruments Plasma multi-collector inductively coupled plasma mass spectrometer. Full details of the method employed are provided in *refs S18–S19*. The isotope activity ratios used to determine each age are shown in Table S2. Most of the age analyses were performed on leftover powders from the high-resolution stable isotope measurements. Depth-age models for each stalagmite segment are shown in Figure S8, and age-uncertainty-vs-age plots are

shown in Figure S9. Details of the method employed for deriving the age models and age-uncertainty-vs-age plots are described in *refs S1–S2*.

2c. Re-plotting of the Iberian margin proxy record onto a common marine timescale

We compiled an 'Iberian margin stack' comprising SST, planktic and benthic $\delta^{18}O$, deep-water $\delta^{18}O$ and temperatures, pollen, and ice-rafted debris from cores ODP-977A *(refs S21–S22)*, MD95-2042 *(refs S23–S25)* and MD01-2444 *(refs S22, S26)* spanning the period ~75 to ~158 ky (Figure S10). The original age models of these cores, which were independently derived (Figure S10a–c), disagree by up to 15,000 yr through the MIS 6-Termination II period. Each core contains a SST series, which potentially allows the data from all three cores to be tied to a common timescale. We opted to tune MD01-2444 and MD95-2042 to the ODP-977A chronology. The latter was selected as the tuning target because its SST was ultimately the series that was tuned to the Corchia speleothem chronology on account of its structure possessing the best match to Corchia $\delta^{18}O$. Common tuning points to ODP-977A were identified by eye and corresponding vertices were added to the age-depth curves for MD01-2444 and MD95-2042 and moved so as to synchronize the records.

The final tuning result is shown in Figure S10d. We estimate the overall uncertainties from tuning to the ODP-977A record to be better than ±1 ky. Given the close geographic proximity of the three marine cores to one another, it is not surprising that their SST records are structurally very similar at the millennial scale. Importantly, there is excellent agreement between the benthic $\delta^{18}O$ of MD95-2042 and MD01-2444, especially for the point at which the benthic termination commences.

The 'weakest link' in placing the Iberian margin data onto a single timescale is the SST series from MD95-2042, which has a very low sampling resolution (averaging one sample per 1000 yr through the termination, less than half that of ODP-977A and MD01-2444). We refined the SST tuning of MD95-2042 core by optimizing its benthic and planktic patterns with those of nearby core MD01-2444 (Figure S11). Consequently, our tuning of MD95-2042 differs slightly to that of *ref S21*).

2d. Re-plotting of the Iberian margin marine stack onto the Corchia timescale

The Iberian margin marine stack was re-plotted on the radiometric timescale of Corchia by manually tuning the SST record from core ODP-977A (the closest of the Iberian margin drilling sites to the cave) to a refined version of the $\delta^{18}O$ series from stalagmite CC5 using the same manual tuning process described above for the Iberian marine stack. Given the high resolution of the SST record and the exceptional match with the Corchia $\delta^{18}O$, we estimate the wiggle-match error to be no greater than ±0.5 ky.

Although both CC1 and CC5 preserve the glacial termination, CC5 has the greatest detail and the best chronology (Figures S9 and S12). Furthermore, the lamination pattern from CC5 was much better resolved, enabling a more reliable level of precision from the microsampling for isotopic analysis and dating. Comparison between CC1 and CC5 (Figure S12a) shows that both curves are not only very similar but lie well within the combined age uncertainties shown in Figure S9. To develop the best chronology through the termination, we first pattern-matched the $\delta^{18}O$ profile of CC1 to the CC5 depth scale. We then interpolated a common, fixed-increment depth scale for each then calculated a new CC5 age model for the period spanning the growth of CC1 (128-149 ky) based on the error-weighted mean of each pair of ages (and their corresponding uncertainties derived from the Monte Carlo modeling described in *refs S1* and *S2*) for each depth increment. The resulting series (Figure S12b) captures the greater structural detail of the CC5 $\delta^{18}O$, *and* utilizes the extra radiometric ages from CC1 to produce a time series with age uncertainties <1.5 ky through the entire termination. This refined CC5 series was used to tune the ODP-977A SST to the Corchia radiometric timescale. The total age uncertainties reported in the main text for specific paleoclimatic events between 128 and 145 ky represent the combined radiometric age error from Figure S12b plus ±1.5 ky (1 ky plus ±0.5 ky) from the two tuning stages described above, combined in quadrature. The resulting Corchia tuning of the marine stack produces little change in the magnitude of sedimentation rates compared to rates based on the ODP-977A timescale (Figure S13); the only major differences relate to phase, as expected.

Finally, it is worth noting that tuning the marine record to the Corchia $\delta^{18}O$ by using the planktic $\delta^{18}O$ as the tuning target is an entirely plausible alternative given that both planktic $\delta^{18}O$ and speleothem $\delta^{18}O$ are driven by source water $\delta^{18}O$ and temperature changes. Indeed, using the ODP-977A planktic $\delta^{18}O$ as the tuning target produces a good pattern match with CC5 $\delta^{18}O$ (Figure S14). However, when the age model of the marine stack is subsequently revised, a number of counterintuitive relationships are produced between the multi-proxy speleothem record and regional temperatures (Figure S15). For example, the period of depressed SSTs associated with H11 shows Corchia (CC5) growth rates increasing and $\delta^{13}C$ decreasing (Figure S15, upper right panel), trends one would normally associate with a warming interval. Furthermore, trace element patterns are incongruent with temperature changes (Fig S15, upper left panel). Given the good agreement between Corchia $\delta^{18}O$, $\delta^{13}C$, growth rates, Mg, and U, use of the planktic $\delta^{18}O$ as the tuning target produces good, but theoretically unsupported associations between these parameters and planktic $\delta^{18}O$. On the other hand, there is good scientific reasoning why CC5 growth rates, $\delta^{13}C$ and trace element patterns should follow SST, particularly given the likely effect of SST on evaporation, moisture advection and rainfall at a site where orographic effects are significant. Hence, we regard SST rather than the planktic $\delta^{18}O$ series is the appropriate tuning target for Corchia $\delta^{18}O$.

4. SUPPORTING FIGURES

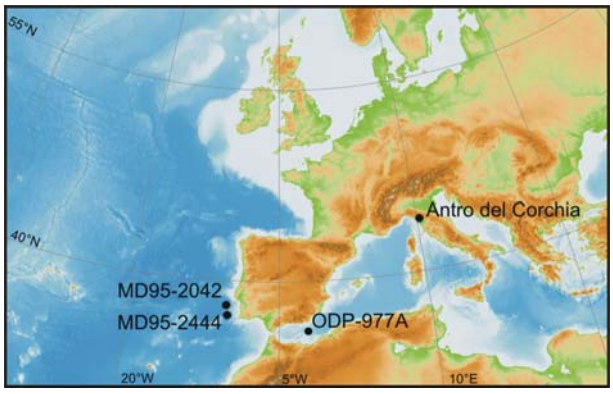

Figure S1: Location of Corchia Cave and North Atlantic marine-core sites mentioned in the text.

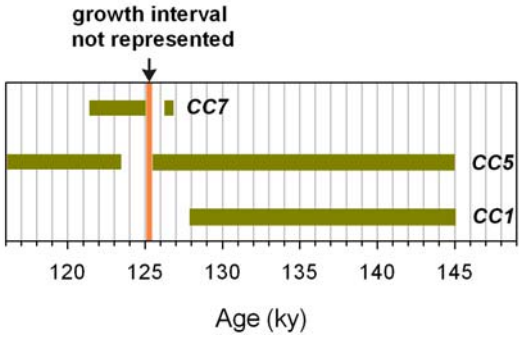

Figure S2: Growth coverage of the three Corchia speleothems.

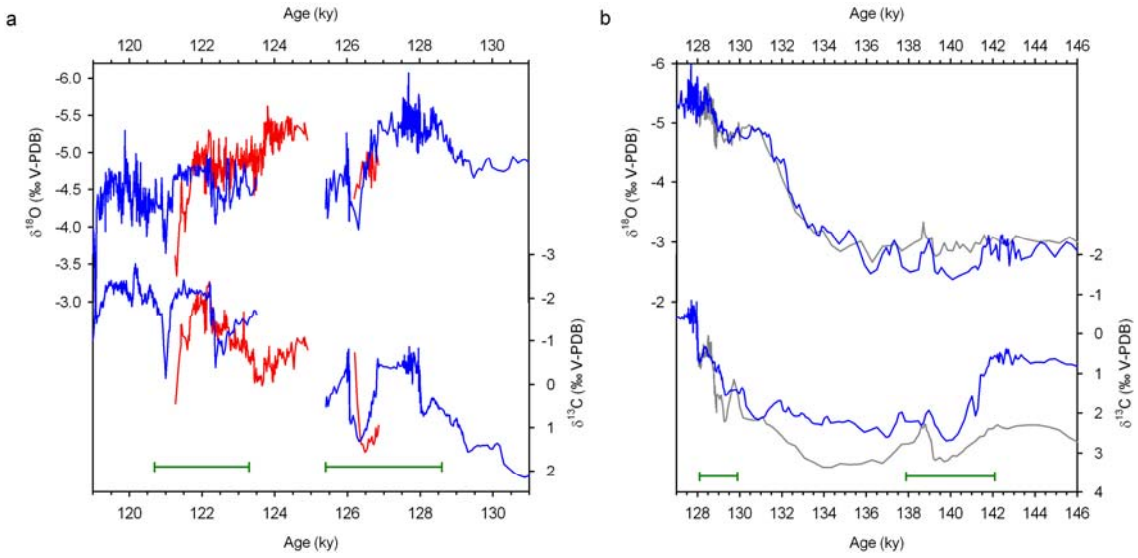

Figure S3: Stable oxygen and carbon isotope variations through overlapping time intervals. (a) CC5 (blue) and CC7 (red); (b) CC5 (blue) and CC1 (gray). Error bars show the maximum ±2σ age uncertainties at various points through these intervals. Offsets between paired isotope series are well within these age-error envelopes.

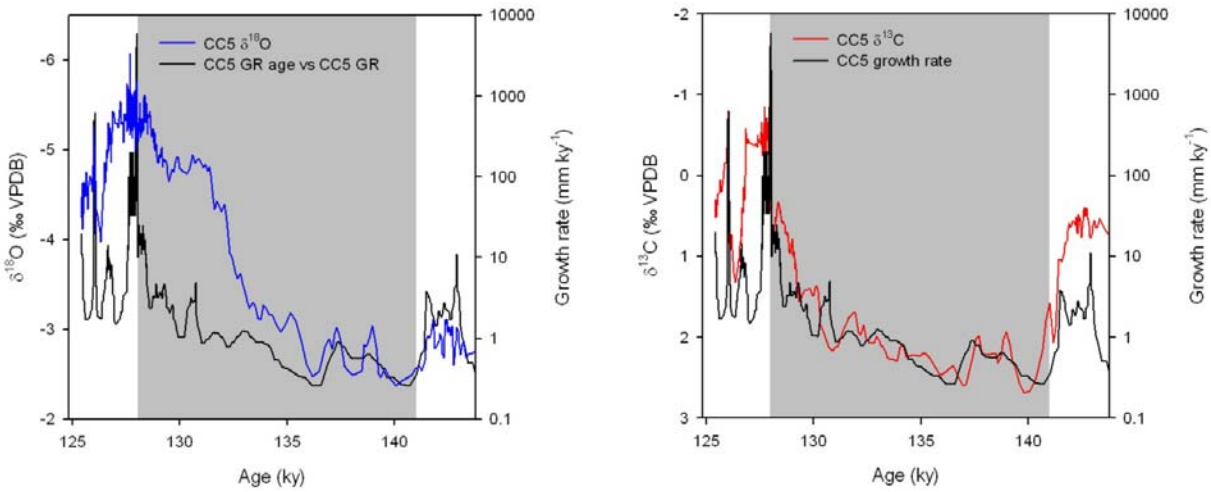

Figure S4: Growth rates versus (a) $\delta^{18}O$ and (b) $\delta^{13}C$ through T-II (approximate duration shown by gray panel)..

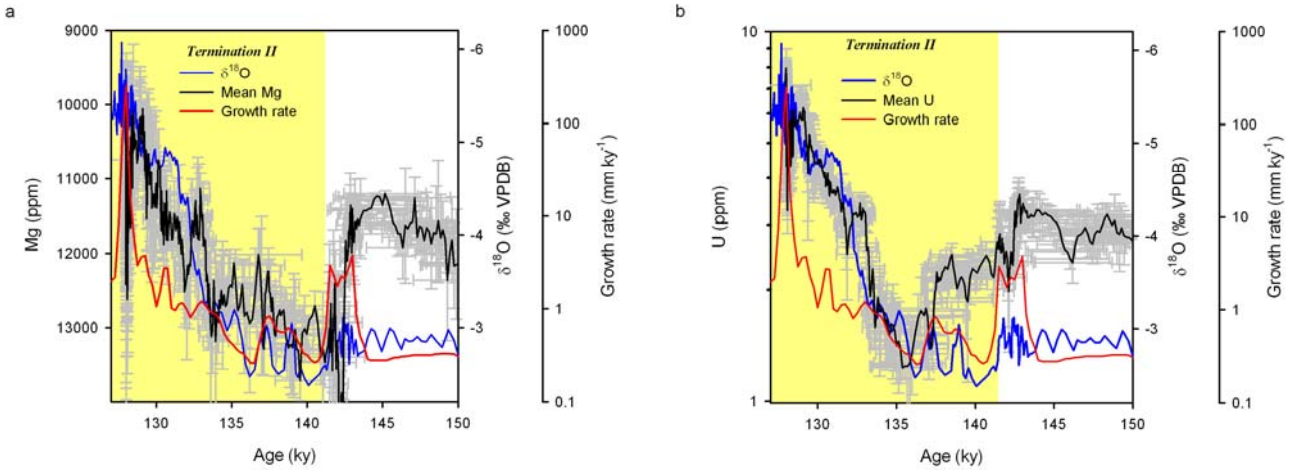

Figure S5: Mean Mg (a) and U (b) concentrations versus CC5 $\delta^{18}O$ and growth rates. Gray vertical error bars are concentration uncertainties from the two sets of scan data, whilst the horizontal error bars are the equivalent age uncertainties (derived from the CC5 depth-age modeling) on transferring the trace element depth scale to the stable isotope depth scale and employing a maximum offset error between the series of ± 0.75 mm. Growth rates represent mean values through 250-yr increments and are plotted on a log scale. U is also plotted on a log scale.

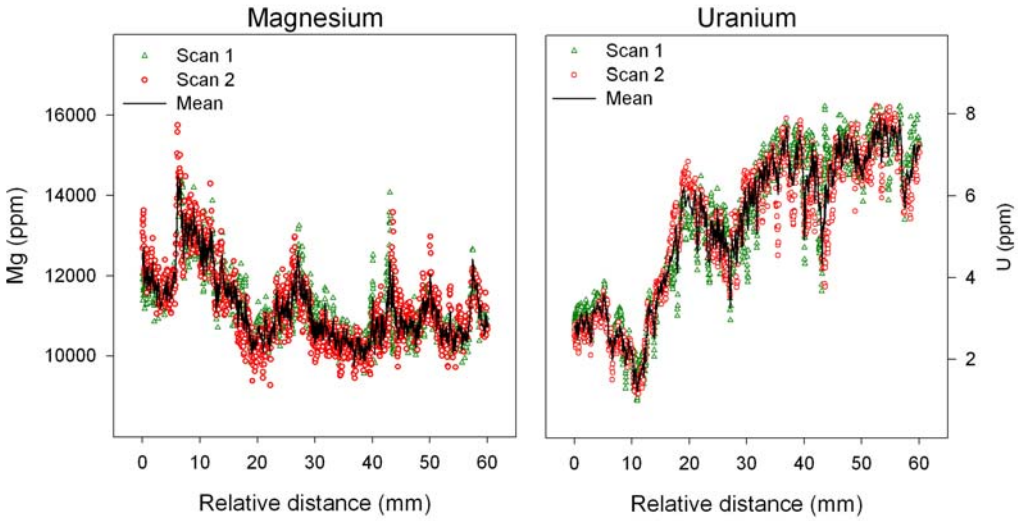

Figure S6: Mg and U data from replicate scan lines (red and green symbols), with the mean value represented by solid black lines.

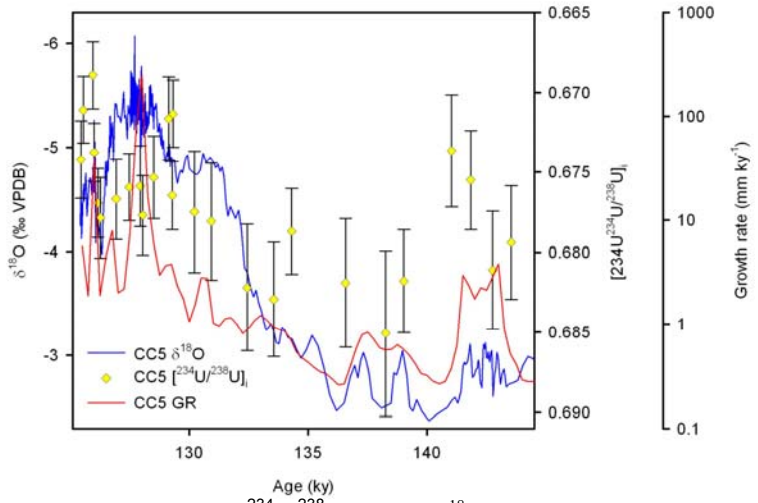

Figure S7: Initial uranium isotope activity ratios $[^{234}U/^{238}U]_i$ versus $\delta^{18}O$ (blue) and growth rate (red) from CC5. Note that the $[^{234}U/^{238}U]_i$ have been calculated retrospectively using model ages and 95% uncertainties (as determined by the Monte Carlo depth-age modeling process – see below) assigned to the age data point depths.

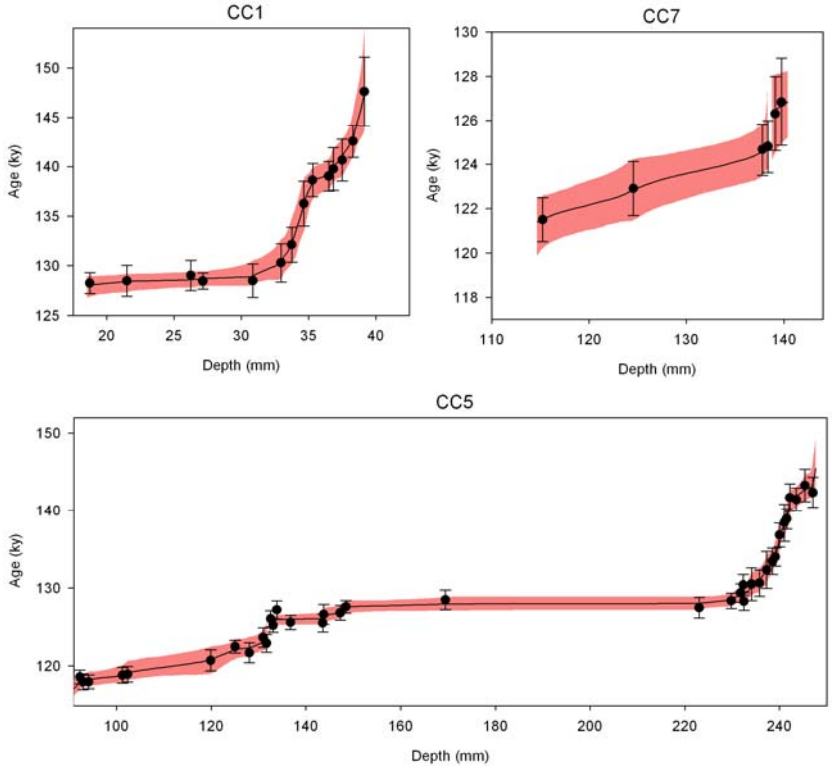

Figure S8: Age model and 95% uncertainty envelopes for each stalagmite. Symbols and error bars on each plot are the U-Th ages and their 95% uncertainties.

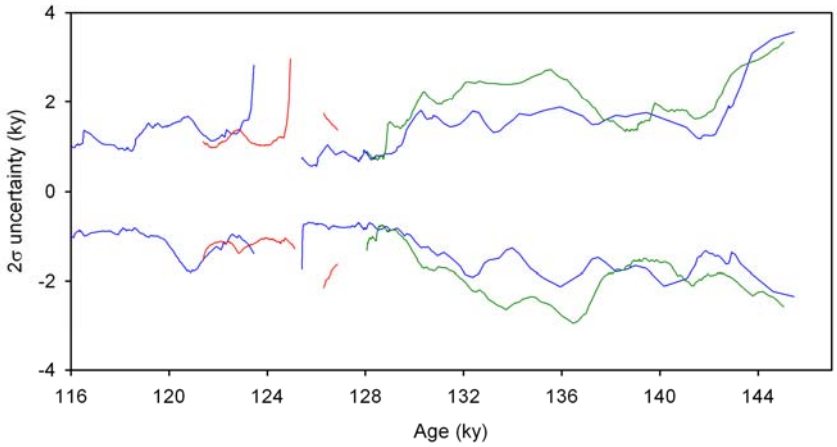

Figure S9: Age-uncertainty-versus-age plots for CC1 (green), CC5 (blue) and CC7 (red).

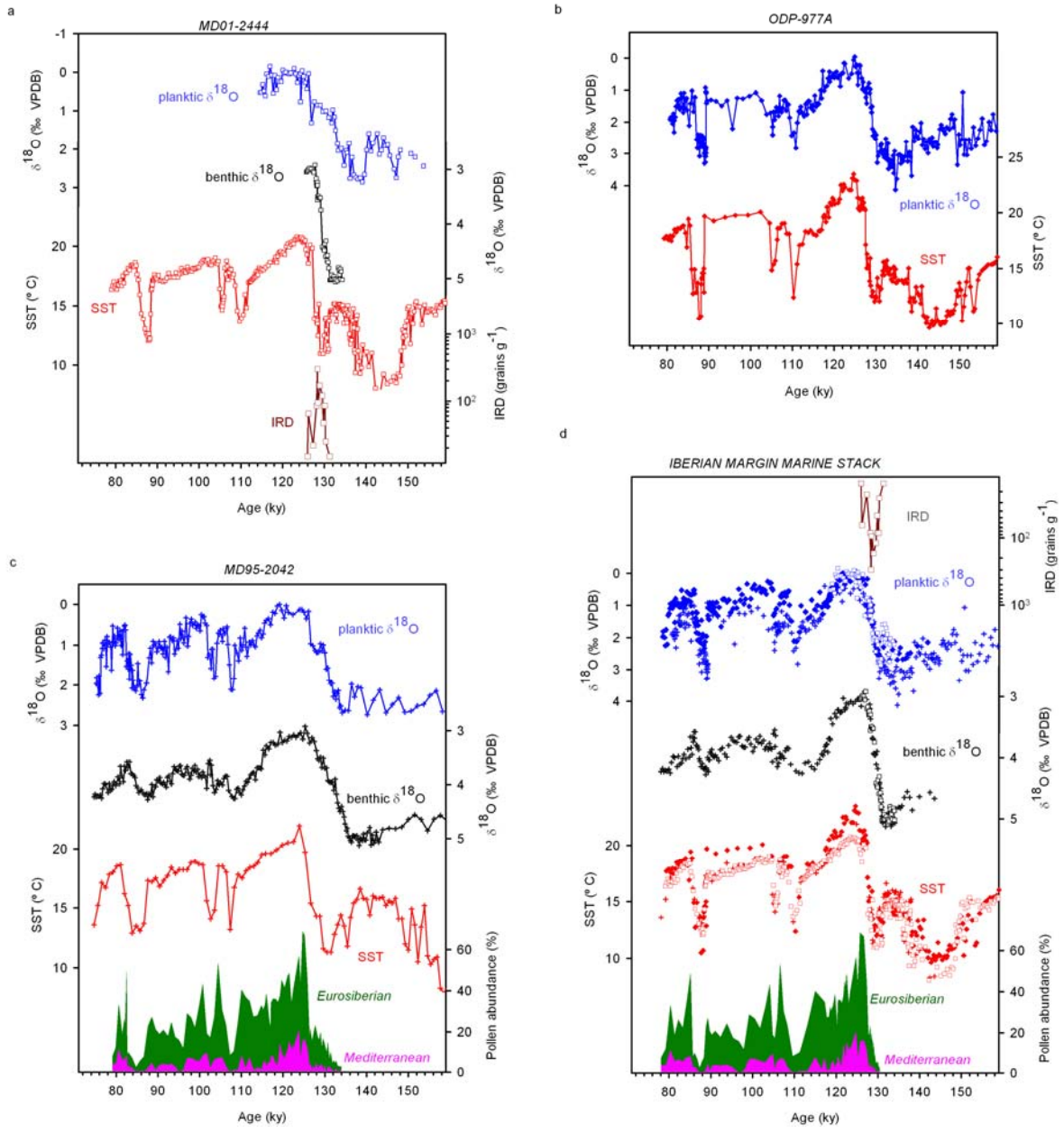

Figure S10: Climate proxy data from Iberian margin cores from Termination II to the early last glacial. In (a) to (c) the data are plotted on their independent timescales, whilst for (d) the composite data are plotted on a common (ODP-977A – *ref. S21*) timescale. (a) MD01-2444: planktic and benthic $\delta^{18}O$, and ice-rafted debris on the timescale of *ref. S26* and $U^{37'}_{k}$ alkenone sea-surface temperatures (SSTs) on the timescale of *ref. S21*. (b) ODP-977A: planktic $\delta^{18}O$ and $U^{37'}_{k}$ alkenone-based sea-surface temperatures (SSTs) on the timescale of *ref. S21*. (c) MD95-02042: benthic and planktic $\delta^{18}O$, abundance of humid-temperate pollen and $U^{37'}_{k}$ alkenone sea-surface temperatures (SSTs) on the timescale of *ref. S23*. (d) Series from (a) to (c) plotted on the common timescale of ODP-977A (*ref. S21*) using the ODP-977A SST as the tuning target.

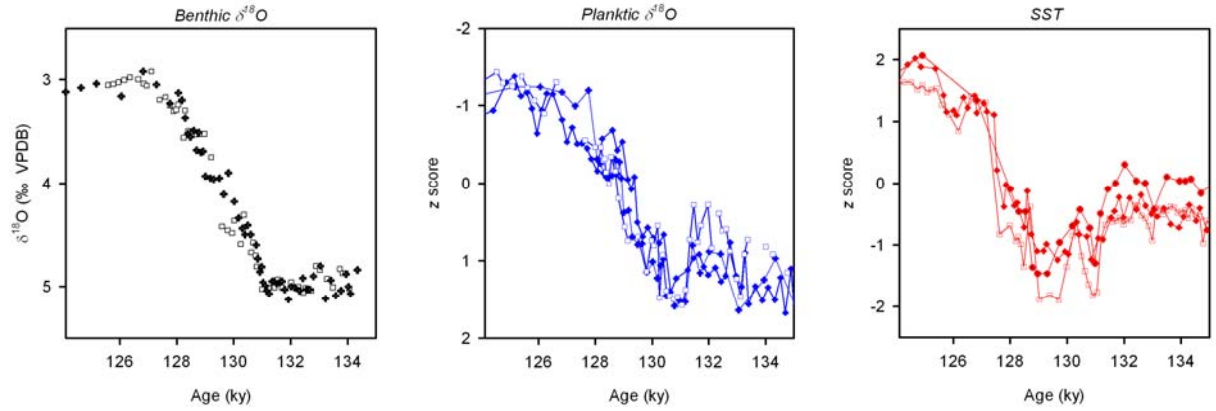

Figure S11: Tuning detail through Termination II for benthic $\delta^{18}O$ (left), planktic $\delta^{18}O$ (middle) and SST (right). All cores (MD01-1444: open squares; MD95-2042: crosses; ODP-977A: solid diamonds) are plotted on the ODP-977A timescale of ref S21. Note that planktic $\delta^{18}O$ and SST are plotted as standard deviation units (*z* scores).

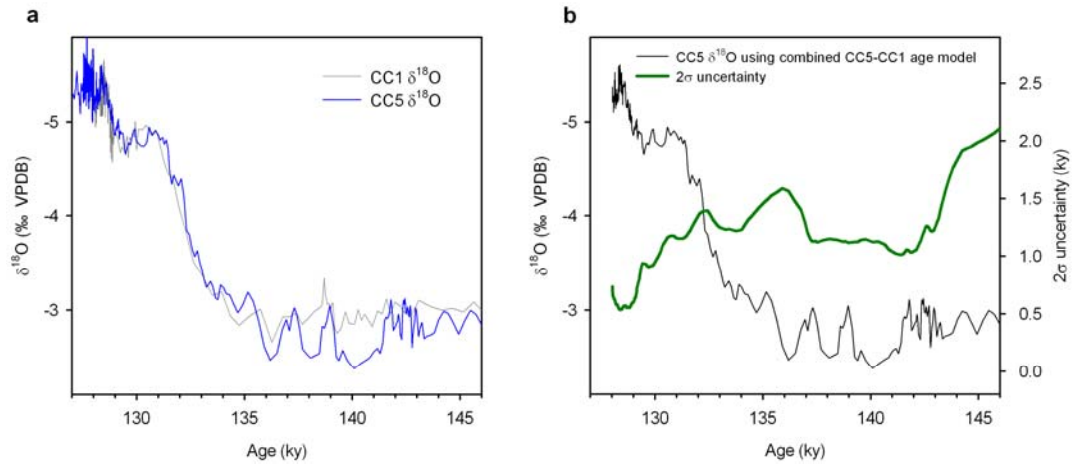

Figure S12: Left: Detailed comparison between CC1 and CC5 $\delta^{18}O$ records, showing good agreement between the two profiles given the age uncertainties shown in Figure S9. Right: Re-plotted CC5 $\delta^{18}O$ using an age scale that combined both individual age models. Note the reduced age uncertainties (green line) resulting from the combined age model.

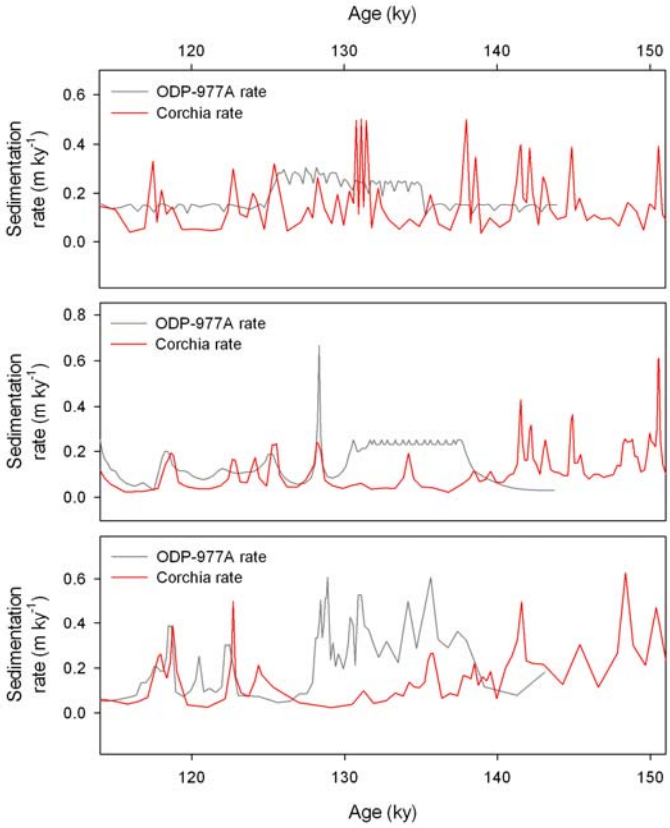

Figure. S13: Comparison of marine sedimentation rates between the ODP-977A and Corchia timescales: MD01-2444 (top), ODP-977A (middle) and MD95-2042 (bottom),

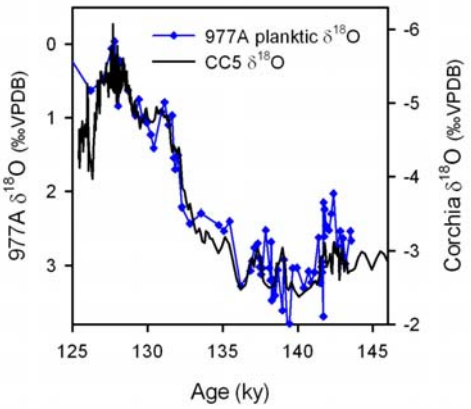

Figure S14: ODP-977A planktic $\delta^{18}O$ tuned to the Corchia chronology using the speleothem $\delta^{18}O$.

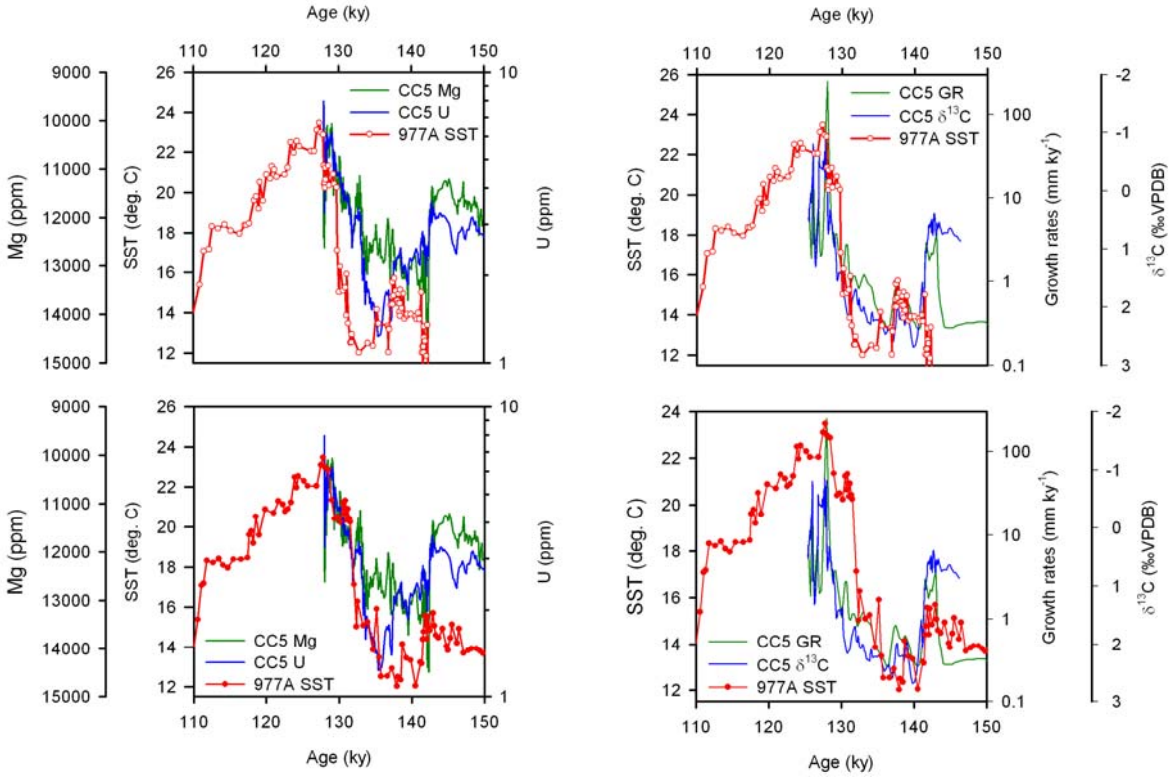

Figure S15: ODP-977A SST versus various Corchia (CC5) speleothem climate proxies. The upper two panels show ODP-977A SST tied to the Corchia chronology using the planktic $\delta^{18}O$ as the tuning target (Figure S14), whereas the lower two panels show the ODP-977A SST tied to the Corchia chronology using SST as the tuning target (Figure 2 of the main article). CC5 growth rates, $\delta^{13}C$ and trace element variations are more closely aligned to the latter SST series.

4. SUPPORTING TABLES

Table S1: Depths, age ranges, and numbers of analyses for each stalagmite segment used in this study.

Stalagmite	*Segment depth range (mm)*	*Segment age range (ka)*	*$\delta^{18}O$ & $\delta^{13}C$ analyses*	*U/Th ages used in final age model*
CC1	18.45 – 39.35	128.0 – 145.0	210	14
CC5	121.25 – 249.75	119.0 – 123.5 125.4 – 145.0	993	35
CC7	114.70 – 138.60 138.70 – 145.60	121.4 – 125.0 126.2 – 126.8	259	7

Table S2: U-Th age data for each Corchia stalagmite. Notes: where given, uncertainties are for the last reported digits and are 95% external confidence intervals. Sample number is asterisked where excluded as an outlier from the age-depth models. Mass (g): mass of sample used for analysis, "n.d." if not recorded. "U ng g^{-1}" is the uranium content of sample, "n.d." if not calculated. "Depth mm" is total stalagmite extension from sample location to tip. Activity ratio determination is as described in *ref. S18* and the supplementary materials of *ref S1*. "Age ky" is the corrected age calculated according to equation 1 of *ref. S19* using the half-lives specified in *ref. S18* and an assumed initial [^{230}Th/^{232}Th] of 1.5 ± 1.5. "[^{234}U/^{238}U]$_i$" is the reconstructed ^{234}U/^{238}U at time of sample formation given its calculated age. Heavy lines denote the position of hiatuses in CC5 and CC7.

Samples	Mass g	U ng g^{-1}	Depth mm	[^{230}Th/^{238}U]	[^{234}U/^{238}U]	[^{232}Th/^{238}U]	[^{230}Th/^{232}Th]	Age ky	[^{234}U/^{238}U]$_i$
CC1 773	0.0020	4654	18.75 (0.20)	0.5086 (16)	0.7722 (16)	0.0000382 (014)	13309	128.3 (1.1)	0.6722 (30)
CC1-503	n.d.	n.d.	21.50 (0.20)	0.5083 (26)	0.7711 (19)	0.0000353 (017)	14391	128.5 (1.6)	0.6705 (38)
CC1-508	n.d.	n.d.	26.25 (0.20)	0.5102 (25)	0.7721 (17)	0.0000421 (015)	12110	129.0 (1.5)	0.6712 (34)
CC1 511-513	0.0083	6563	27.15 (0.30)	0.5097 (12)	0.7726 (13)	0.0000060 (003)	84996	128.5 (0.8)	0.6727 (24)
*CC1-528	n.d.	n.d.	28.75 (0.20)	0.5090 (22)	0.7746 (22)	0.0000418 (083)	12176	127.6 (1.4)	0.6758 (41)
CC1-549	n.d.	n.d.	30.85 (0.20)	0.5115 (28)	0.7753 (17)	0.0000284 (024)	18016	128.5 (1.7)	0.6761 (34)
CC1-570	n.d.	n.d.	32.95 (0.20)	0.5153 (31)	0.7754 (25)	0.0000914 (049)	5640	130.3 (1.9)	0.6749 (47)
CC1-578	n.d.	n.d.	33.75 (0.40)	0.5214 (28)	0.7794 (21)	0.0001339 (148)	3895	132.1 (1.8)	0.6786 (41)
CC1-587	n.d.	n.d.	34.65 (0.20)	0.5295 (35)	0.7797 (22)	0.0000412 (030)	12850	136.3 (2.2)	0.6756 (45)
CC1 593-594	0.0057	3388	35.30 (0.30)	0.5359 (26)	0.7821 (15)	0.0000156 (013)	34316	138.6 (1.7)	0.6772 (32)
CC1 605-606	0.0033	2841	36.50 (0.30)	0.5374 (22)	0.7830 (19)	0.0000880 (031)	6109	139.0 (1.5)	0.6782 (37)
CC1-609	n.d.	n.d.	36.85 (0.20)	0.5384 (33)	0.7827 (22)	0.0003858 (065)	1396	139.7 (2.2)	0.6770 (45)
CC1 615-616	0.0027	4151	37.50 (0.30)	0.5422 (33)	0.7854 (16)	0.0000288 (023)	18812	140.6 (2.1)	0.6803 (35)
CC1 623-624	0.0048	3600	38.30 (0.30)	0.5431 (20)	0.7826 (22)	0.0001365 (010)	3978	142.6 (1.6)	0.6743 (44)
CC1-632	n.d.	n.d.	39.15 (0.20)	0.5526 (45)	0.7839 (36)	0.0007375 (216)	749	147.6 (3.5)	0.6716 (79)
CC5d 76-80	0.0054	4280	92.25 (0.60)	0.4870 (15)	0.7689 (14)	0.0000227 (006)	21409	118.6 (0.9)	0.6765 (26)
CC5d 73	0.0026	3347	92.87 (0.20)	0.4875 (16)	0.7714 (17)	0.0000245 (015)	19901	118.0 (1.0)	0.6805 (32)
CC5d 61-65	0.0071	4458	94.10 (0.50)	0.4852 (14)	0.7683 (14)	0.0000140 (005)	34724	118.0 (0.9)	0.6763 (25)
CC5-288	0.0102	4902	101.25 (1.50)	0.4885 (15)	0.7704 (21)	0.0000146 (029)	33360	118.8 (1.0)	0.6784 (35)
CC5c 4+6	0.0028	3860	102.31 (0.40)	0.4884 (18)	0.7699 (13)	0.0000355 (043)	13747	119.0 (1.0)	0.6776 (25)
CC5-4R	0.0129	5755	119.90 (1.50)	0.4932 (26)	0.7713 (15)	0.0000232 (011)	21250	120.7 (1.3)	0.6781 (29)
CC5a 437-439	0.0029	5026	125.05 (0.40)	0.4953 (13)	0.7697 (13)	0.0000474 (010)	10453	122.5 (0.8)	0.6740 (24)
CC5a 467-469	0.0032	3224	128.05 (0.40)	0.4969 (22)	0.7738 (17)	0.0000852 (014)	5834	121.7 (1.3)	0.6803 (32)
CC5c 210-212	n.d.	n.d.	130.95 (0.40)	0.4989 (21)	0.7710 (16)	0.0001161 (012)	4297	123.6 (1.2)	0.6748 (30)
CC5c 203+205	0.0030	4961	131.65 (0.40)	0.4976 (17)	0.7712 (19)	0.0000155 (012)	32159	122.9 (1.1)	0.6758 (35)
CC5f 4+6	0.0056	3200	132.55 (0.40)	0.5038 (14)	0.7713 (18)	0.0000370 (009)	13629	126.0 (1.1)	0.6731 (34)
CC5f 9-11	n.d.	n.d.	133.05 (0.40)	0.5010 (14)	0.7697 (14)	0.0000696 (014)	7201	125.2 (0.9)	0.6716 (26)
CC5f 17-19	n.d.	n.d.	133.85 (0.40)	0.5031 (18)	0.7676 (16)	0.0000253 (015)	19917	127.2 (1.2)	0.6667 (30)
CC5a 572-575	0.0036	4870	136.75 (0.50)	0.5033 (14)	0.7719 (13)	0.0000176 (007)	28544	125.6 (0.9)	0.6742 (24)
CC5a 504-506	0.0031	3320	143.55 (0.40)	0.5051 (19)	0.7743 (15)	0.0000306 (010)	16493	125.5 (1.1)	0.6777 (28)
CC5-328	0.0080	3612	143.75 (1.50)	0.5076 (20)	0.7747 (18)	0.0000185 (019)	27391	126.6 (1.3)	0.6774 (34)
CC5a 327-331	0.0030	7135	147.25 (0.50)	0.5077 (13)	0.7744 (17)	0.0001352 (012)	3755	126.8 (0.9)	0.6766 (31)
CC5-333	n.d.	n.d.	148.45 (1.50)	0.5091 (11)	0.7742 (13)	0.0000049 (004)	104620	127.6 (0.8)	0.6758 (25)
CC5-6	0.0078	6991	169.45 (1.50)	0.5118 (19)	0.7744 (17)	0.0016790 (038)	305	128.5 (1.3)	0.6753 (32)
CC5-877	n.d.	n.d.	223.05 (0.20)	0.5103 (21)	0.7760 (17)	0.0000487 (013)	10481	127.5 (1.3)	0.6785 (33)
*CC5 834-836	0.0039	7194	227.20 (0.40)	0.5141 (19)	0.7744 (15)	0.0004075 (354)	1262	130.0 (1.2)	0.6739 (30)
CC5-31	0.0114	4559	229.80 (0.50)	0.5112 (14)	0.7745 (16)	0.0000230 (014)	22266	128.4 (1.0)	0.6757 (29)
CC5-32	0.0075	6185	231.80 (1.50)	0.5113 (17)	0.7723 (18)	0.0000300 (015)	17067	129.4 (1.2)	0.6716 (35)

Samples	Mass g	U ng g^{-1})	Depth mm	$[^{230}Th/^{238}U]$	$[^{234}U/^{238}U]$	$[^{232}Th/^{238}U]$	$[^{230}Th/^{232}Th]$	Age ky	$[^{234}U/^{238}U]_i$
CC5 784-783	0.0021	4603	232.35 (0.30)	0.5157 (22)	0.7756 (15)	0.0000286 (013)	18023	130.4 (1.3)	0.6752 (30)
CC5-30	0.0159	5553	232.50 (1.50)	0.5095 (18)	0.7726 (15)	0.0000084 (006)	60376	128.3 (1.1)	0.6730 (29)
CC5-766	n.d.	n.d.	234.10 (0.20)	0.5167 (32)	0.7770 (26)	0.0000322 (072)	16052	130.5 (2.1)	0.6770 (50)
CC5-749	n.d.	n.d.	235.80 (0.20)	0.5180 (25)	0.7778 (23)	0.0005451 (069)	950	130.6 (1.7)	0.6782 (44)
CC5-734	n.d.	n.d.	237.30 (0.20)	0.5238 (38)	0.7815 (23)	0.0000448 (028)	11698	132.3 (2.4)	0.6818 (46)
CC5-722	n.d.	n.d.	238.50 (0.20)	0.5267 (25)	0.7827 (22)	0.0000641 (024)	8214	133.4 (1.7)	0.6823 (43)
CC5-7R	0.0220	2401	239.15 (1.50)	0.5262 (18)	0.7803 (14)	0.0000818 (033)	6429	134.0 (1.2)	0.6788 (27)
CC5-707	n.d.	n.d.	240.00 (0.20)	0.5342 (21)	0.7840 (23)	0.0001393 (034)	3834	136.8 (1.5)	0.6815 (43)
CC5 696+697	n.d.	n.d.	241.05 (0.30)	0.5392 (30)	0.7869 (33)	0.0000842 (023)	6406	138.4 (2.4)	0.6842 (65)
CC5-136	0.0106	2852	241.50 (1.50)	0.5389 (17)	0.7853 (17)	0.0000256 (014)	21060	138.9 (1.3)	0.6817 (34)
CC5-685	n.d.	n.d.	242.20 (0.20)	0.5400 (23)	0.7809 (22)	0.0001363 (031)	3961	141.7 (1.8)	0.6725 (46)
CC5 673-671	0.0043	3549	243.55 (0.40)	0.5416 (18)	0.7829 (19)	0.0002848 (020)	1902	141.5 (1.5)	0.6758 (39)
CC5-653	n.d.	n.d.	245.40 (0.20)	0.5476 (29)	0.7871 (23)	0.0000607 (092)	9019	143.3 (2.1)	0.6800 (50)
CC5 638-636	0.0029	3084	247.05 (0.40)	0.5460 (28)	0.7864 (21)	0.0000825 (031)	6621	142.4 (1.9)	0.6802 (43)
CC7 635-639	0.0049	3651	115.25 (0.60)	0.4950 (14)	0.7719 (18)	0.0000443 (018)	11179	121.5 (1.0)	0.6779 (32)
*CC7 688-692	0.0037	3372	120.55 (0.60)	0.4956 (16)	0.7678 (17)	0.0000405 (015)	12233	123.4 (1.0)	0.6702 (32)
CC7 728-732	0.0036	2203	124.55 (0.60)	0.4966 (20)	0.7701 (20)	0.0000414 (016)	11986	122.9 (1.2)	0.6743 (35)
CC7-11	n.d.	n.d.	137.80 (1.50)	0.5030 (19)	0.7732 (17)	0.0000450 (016)	11189	124.7 (1.2)	0.6771 (32)
CC7 804-806	0.0094	6547	138.35 (0.40)	0.5015 (20)	0.7714 (16)	0.0000176 (007)	28495	124.8 (1.2)	0.6743 (30)
CC7 331-332	0.0027	2724	139.10 (0.30)	0.5076 (25)	0.7750 (26)	0.0005186 (102)	979	126.3 (1.7)	0.6782 (49)
CC7-325	n.d.	n.d.	139.75 (0.20)	0.5053 (35)	0.7711 (22)	0.0001343 (030)	3762	126.8 (2.0)	0.6721 (43)

5. SUPPORTING REFERENCES AND NOTES

1. Drysdale, R., et al. Stalagmite evidence for the onset of the Last Interglacial in southern Europe at 129 ± 1 ka. *Geophysical Research Letters* 32, L24708, (2005) doi:10.1029/2005GL024658.

2. Drysdale, R.N. et al. Stalagmite evidence for the precise timing of North Atlantic cold events during the early last glacial, *Geology* 35, 77-80 (2007).

3. Drysdale, R.N. et al. Palaeoclimatic implications of the growth history and stable isotope ($\delta^{18}O$ and $\delta^{13}C$) geochemistry of a Middle to Late Pleistocene stalagmite from central-western Italy. *Earth and Planetary Science Letters* 227, 215–229, (2004). doi: 10.1016/j.epsl.2004.09.010.

4. McDermott, F. Palaeo-climate reconstruction from stable isotope variations in speleothems: a review. *Quaternary Science Reviews* 23, 901–918 (2004).

5. Lachinet, M.S. Climatic and environmental controls on speleothem oxygen-isotope values. *Quaternary Science Reviews* 28, 412-432 (2008).

6. Piccini L. et al. The environmental features of the Monte Corchia cave system (Apuan Alps, central Italy) and their effects on speleothem growth. *International Journal of Speleology* 37, 153-173 (2008).

7. Bard, E., et al. Hydrological conditions over the western Mediterranean basin during the deposition of the cold Sapropel 6 (ca. 175 kyr BP). *Earth and Plantary Science Letters* 202, 481-494 (2002).

8. Longinelli, A. et al. Isotopic composition of precipitation in Northern Italy: reverse effect of anomalous climatic events. Journal of Hydrology 329, 471-476 (2006).

9. Zanchetta, G. et al. Enhanced rainfall in the Western Mediterranean during deposition of sapropel S1: stalagmite evidence from Corchia cave (Central Italy). *Quaternary Science Reviews* 26, 279-286 (2007).

10. Rohling, E. et al. African monsoon variability during the previous interglacial maximum. Earth and Planterary Science Letters 202, 61-75 (2002).

11. Kaufmann, G. & Dreybrodt, W. Stalagmite growth and palaeo-climate: an inverse approach. *Earth and Planetary Science Letters* 224, 529-545 (2004).

12. Genty. D., Baker, A., Vokal, B. Intra- and inter-annual growth rate of modern stalagmites. *Chemical Geology* 176, 191-212 (2001).

13. Desmarchelier, J., Hellstrom, J. and McCulloch, M. Rapid trace element analysis of speleothems by ELA-ICP-MS. *Chemical Geology* 231, 102-117 (2006).

14. Treble, P., Shelley, J.M.G., Chappell, J. Comparison of high-resolution subannual records of trace elements in a modern (1911–1992) speleothem with instrumental climate data from southwest Australia. *Earth and Planetary Science Letters* 216, 141–153 (2003).

15. Fairchild, I.C. & Treble, P.C. Trace elements in speleothems as recorders of environmental change. *Quaternary Science Reviews* 28, 449-468 (2009).,

16. Drysdale, R; Zanchetta, G; Hellstrom, J; Maas, R; Fallick, A. Major climate events of the last 130 ka recorded in Corchia Cave (Italy) speleothems. EGU2007 General Assembly, abstract EGU2007-A-01137 (2007)

17. Langmuir, D. Uranium solution-mineral equilibria at low temperatures with applications to sedimentary ore deposits. *Geochimica et Cosmochimica Acta* 42, 547-569 (1978).

18. Hellstrom, J.C. and M.T. McCulloch. Multi-proxy constraints on the climatic significance of trace element records from a New Zealand speleothem, *Earth Planet. Sci. Lett. 179*, 287-297 (2000).

19. Hellstrom, J.C. Rapid and accurate U/Th dating using parallel ion-counting multi-collector ICP-MS. *Journal of Analytical Atomic Spectrometry* 18, 1346–1351 (2003). doi: 10.1039/b308781f.

20. Hellstrom, J.C. U–Th dating of speleothems with high initial ^{230}Th using stratigraphical constraint. *Quaternary Geochronology* 1*,* 289-295 (2006).

21. Martrat, B. et al. Four climate cycles of recurring deep and surface water destabilizations on the Iberian margin. *Science* 317, 502-507 (2007).

22. Martrat, B. et al. Abrupt temperature changes in the Western Mediterranean over the past 250,000 years. *Science* 306, 1762–1765 (2004).

23. Sánchez Gõni, M.E. et al. High resolution palynological record off the Iberian margin: direct land-sea correlation for the Last Interglacial complex. *Earth and Planetary Science Letters* 171, 123-137. (1999).

24. Sánchez Goñi, M.F. Introduction to climate and vegetation in Europe during MIS 5. In: Sirocko, F., Claussen, M., Sánchez Goñi, M.F. & Litt, T. (eds.) *The climate of past interglacials*. Elsevier, 197-205 (2007).

25. Pailler, D., Bard, E. High frequency palaeoceanographic changes during the past 140,000 yr recorded by the organic matter in sediments of the Iberian margin: *Palaeogeography, Palaeoclimatology, Palaeogeography* 181, 431–452 (2002). doi: 10.1016/S0031-0182(01)00444-8.

26. Skinner, L., Shackleton, N.J. Deconstructing Terminations I and II: revisiting the glacioeustatic paradigm based on deep-water temperature estimates. *Quaternary Science Reviews* 25*,* 3312-3321 (2006).